



## Structural and magnetic characterization of barbosalite $\text{Fe}_3(\text{PO}_4)_2(\text{OH})_2$

M. Poienar <sup>a</sup>, F. Damay <sup>b</sup>, J. Rouquette <sup>c</sup>, V. Ranieri <sup>c</sup>, S. Malo <sup>d</sup>, A. Maignan <sup>d,\*</sup>, E. Elkaïm <sup>e</sup>, J. Haines <sup>c</sup>, C. Martin <sup>d</sup>



<sup>a</sup> National Institute for Research and Development in Electrochemistry and Condensed Matter, Renewable Energies - Photovoltaic Laboratory, Str. Dr. A. Păunescu Podeanu, nr.144, 300569, Timișoara, Timiș, Romania

<sup>b</sup> Laboratoire Léon Brillouin, CEA-CNRS UMR 12, 91191, GIF-SUR-YVETTE, CEDEX, France

<sup>c</sup> Institut Charles Gerhardt UMR CNRS 5253, Université Montpellier II, Place Eugène Bataillon, cc1503, 34095, Montpellier, Cedex 5, France

<sup>d</sup> Laboratoire CRISMAT, Normandie Univ, ENSICAEN, UNICAEN, CNRS, 14000, Caen, France

<sup>e</sup> Synchrotron Soleil, L'Orme des Merisiers, BP 4891192, GIF-sur-YVETTE CEDEX, Saint-Aubin, France

### ARTICLE INFO

#### Keywords:

Barbosalite  
Crystal structure  
Magnetic order

### ABSTRACT

Single crystals and polycrystalline samples of barbosalite  $\text{Fe}_3(\text{PO}_4)_2(\text{OH})_2$  iron phosphate were successfully synthesized by hydrothermal method at low pressure and temperature. Careful investigations of the crystal structure by high resolution X-ray diffraction and transmission electron microscopy evidence a complex barbosalite framework where trimers of face sharing  $\text{FeO}_6$  octahedra along the  $\langle 110 \rangle$  direction are connected by an additional Fe site, partly occupied. Despite this structural disorder, the spins order in a rather simple magnetic structure below 160 K. The corresponding magnetic point group of  $P2_1$  makes the barbosalite a promising candidate for the design of new multiferroics.

### 1. Introduction

Natural iron hydroxyl phosphates are minerals with a very rich crystal chemistry in connection with complex structures that are able to adapt several contents of Fe, OH or  $\text{H}_2\text{O}$ . The study of such materials, to determine their compositions and to establish relationships between structures, microstructures and functionalities, is often motivated by their applications related to energy and catalysis. For instance,  $\text{Li}_3\text{Fe}_2(\text{PO}_4)_3$  or  $\text{LiFePO}_4$  used as cathode materials in batteries have attracted much attention, according to the Li insertion made possible by the  $\text{Fe}^{3+}/\text{Fe}^{2+}$  redox couple [1–4]. In that respect, the  $\text{Fe}_3(\text{PO}_4)_2(\text{OH})_2$  barbosalite, belonging to the  $P2_1/c$   $\text{MgAl}_2(\text{PO}_4)_2(\text{OH})_2$  lazurite group, has just been recently shown to be less performing than  $\text{LiFePO}_4$  with the possibility to exchange only 0.7 Li at 2.6 V [5]. However, barbosalite exhibits the best catalytic properties of the Fe–P–OH–H system [6,7].

The presence of high spin  $\text{Fe}^{3+}/\text{Fe}^{2+}$  cations in these compounds make them interesting candidates for magnetoelectric properties.  $\text{LiFePO}_4$ , a member of the  $\text{LiMPO}_4$  olivines, is an antiferromagnet with  $T_N \approx 50$  K [8,9] that crystallizes in the same structure as the magnetoelectric members  $\text{LiNiPO}_4$  and  $\text{LiCoPO}_4$  [10,11]. In that context, it becomes worthy to study the magnetic structure of the  $\text{Fe}_3(\text{PO}_4)_2(\text{OH})_2$  barbosalite. This is also motivated by the presence in this structure of Fe

trimers formed by face-shared  $\text{FeO}_6$  octahedra [12,13]. Indeed, the presence of such trimers, in which a ferrous cation is surrounded by two ferric cations, could be involved in the multiferroic behaviour of the  $\text{Fe}_3\text{BO}_5$  ludwigite [14].

G.J. Redhammer et al. [15] have reinvestigated the barbosalite and characterized its magnetic properties, revealing a magnetic transition at  $\approx 160$  K, but the magnetic structure and its temperature dependence are still unknown. In this context, we have undertaken a detailed study of the  $\text{Fe}_3(\text{PO}_4)_2(\text{OH})_2$  barbosalite for its structural and magnetic properties, by using X-ray, neutron and electron diffraction and magnetometry, on both single crystals and polycrystalline samples.

### 2. Experimental section

Two types of hydrothermal synthesis were used, leading to barbosalite crystals with different sizes but with similar structural and physical properties.

- The reactants  $\text{FeCl}_2 \cdot 6\text{H}_2\text{O}$  [1.2096 g],  $\text{FeCl}_3$  [0.9869 g] and  $(\text{NH}_4)_2\text{HPO}_4$  [0.8034 g] were dissolved independently in distilled water by magnetic stirring during 30 min approximatively. The mixtures were transferred to a 63 mL Teflon-lined stainless steel

\* Corresponding author.

E-mail address: [antoine.maignan@ensicaen.fr](mailto:antoine.maignan@ensicaen.fr) (A. Maignan).

autoclave (80% degree of filling) and magnetically stirred at room temperature leading to the formation of a greyish blue precipitate. Lastly, the autoclave was sealed and heated at 220 °C for 72 h. At the end, black green powder was collected by filtration, washed with distilled water and dried at 90 °C for 3 h in air.

(ii)  $\text{Fe}_3(\text{PO}_4)_2(\text{OH})_2$  single crystals of about 5–30  $\mu\text{m}$  dimensions were grown hydrothermally at low pressure and 220 °C from a mixture of  $\text{FeSO}_4 \cdot 7\text{H}_2\text{O}$  [7 g],  $\text{FePO}_4 \cdot 7\text{H}_2\text{O}$  [2.8 g] and  $\text{H}_3\text{PO}_4$  (85%) [2 mL] (for 25 mL  $\text{H}_2\text{O}$  and 60% degree of filling of the 45 mL Teflon-lined autoclave) which was quenched after one week

Room temperature (RT) X-ray powder diffraction (XRPD) data have been collected using a PANalytical diffractometer with  $\text{Co K}\alpha$  radiations [ $5^\circ < 2\theta < 115^\circ$ ]. RT synchrotron X-ray powder diffraction (SXRPD) was carried out on the CRISTAL beamline at SOLEIL, using a wavelength  $\lambda = 0.72613 \text{ \AA}$ . A small amount of sample was crushed and sifted at 63  $\mu\text{m}$  and put in a 0.3 mm quartz capillary. Neutron powder diffraction versus temperature was performed at LLB on the G4.1 diffractometer ( $\lambda = 2.428 \text{ \AA}$ ) from 1.7 to 300 K. Rietveld refinements were performed by means of the Fullprof suite [16], which also includes the BasIreps software used for the representational analysis of the magnetic structure.

A  $5 \times 6 \times 15 \mu\text{m}^3$  octahedral crystal was characterized by X-ray diffraction. Complete sphere-scans with a step width of 0.5° were performed with a Dectris Pilatus detector placed at 34 mm from the sample. Data collection, indexing, reduction and correction for absorption were performed using CrysAlisPro (Oxford Diffraction). Structure determination and refinements were performed using SHELXL-2014/7.31 [17]. WinGX was used for Fourier map.

Transmission electron microscopy (TEM) specimens were prepared by smoothly crushing samples with n-butanol in an agate mortar and

depositing the drops onto a holey carbon grid supported by copper. Electron diffraction (ED) study at RT was carried out, using a JEOL 2010 microscope equipped with tilt-rotation sample holder ( $\pm 50$ ) (operating at 200 kV).

Magnetic properties were studied by collecting magnetization ( $M$ ) in both zero-field-cooling ( $zfc$ ) and field-cooling ( $fc$ ) modes with a SQUID magnetometer (MPMS, Quantum Design) in a magnetic field of 100 Oe, from 5 to 300 K. The magnetic susceptibility is calculated from these data. Magnetization versus magnetic field loops were also collected by using the same equipment at 5, 50, 100, 150 and 180 K, from 0 to +5 T, then to -5 T and then to +5 T.

### 3. Results

#### 3.1. Structural characterizations

The RT SXRPD pattern of the polycrystalline sample can be indexed using the  $P2_1/n$  space group and lattice parameters:  $a = 7.3231 \text{ \AA}$ ,  $b = 7.4687 \text{ \AA}$ ,  $c = 7.4073 \text{ \AA}$  and  $\beta = 118.565^\circ$ , in agreement with the previous reports [5,15]. The barboselite framework is described as consisting of  $\text{Fe}^{3+}\text{-Fe}^{2+}\text{-Fe}^{3+}$  face sharing  $\text{FeO}_6$  octahedra trimers, oriented along the  $\langle 110 \rangle$  direction, and connected together by phosphate tetrahedra [15] (Fig. 1a and b). In this model, two iron sites are necessary to build the structure: Fe1 in 4e Wyckoff position and Fe2 in 2a (0 0 0), corresponding to trivalent and divalent species, respectively (as determined from the average of the Fe–O distances). Fe2 sits at the inversion symmetry of the trimer. Although the refinement of the SXRPD data using this  $P2_1/n$  space group lead to good agreement factors, very weak extra peaks were detected and attributed to a small amount of  $\text{Fe}_4(\text{PO}_4)_3(\text{OH})_3$  [18].

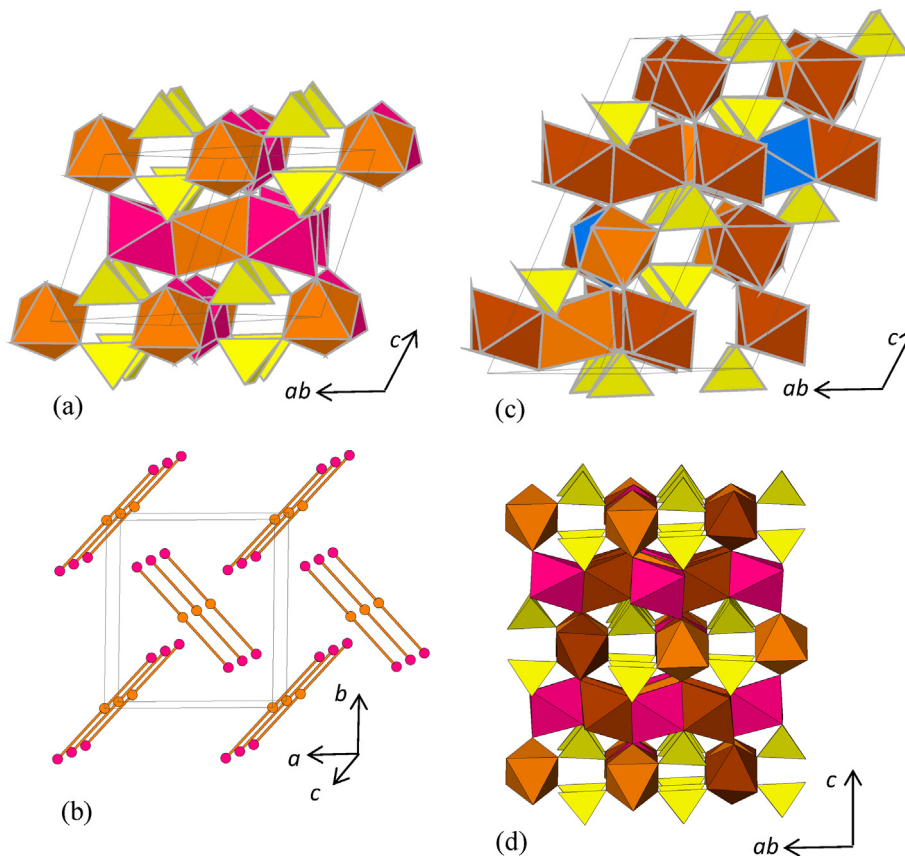


**Fig. 1.** Barboselite structure in the small  $P2_1/n$  space group: (a) showing the  $\text{PO}_4$  tetrahedra (yellow) and  $\text{FeO}_6$  octahedra (red and orange) and (b) highlighting the Fe trimers. Double barboselite structure in the  $P2_1$  space group, the blue octahedra correspond to the additional  $\text{Fe}7$  site (c). Lipscombe structure  $P4_32_12$  (d). (For interpretation of the references to colour in this figure legend, the reader is referred to the Web version of this article.)

To go further in the structural analysis of  $\text{Fe}_3(\text{PO}_4)_2(\text{OH})_2$ , numerous selected area electron diffraction (SAED) patterns were recorded on different crystallites and the reconstruction of the reciprocal space, carried out by tilting around the unique axis  $b^*$ , evidences a  $2_1$  screw axis along  $b$  and a lattice compatible with the parameters reported above (Fig. 2a,b,c). But, whatever the crystallite, from single or polycrystalline samples, none  $(0\ 1\ 0)^*$  ED pattern is compatible with the existence of a  $n$ -glide plane (in Fig. 2b the blue arrows point out the spots incompatible with a  $n$ -glide plane). The main spots are then compatible with the aforementioned lattice parameters and the  $P2_1$  non centrosymmetric space group. Moreover, additional phenomena are observed, like twins as shown in Fig. 2c or super lattice reflections as pointed out by blue arrows in the  $(1\ 0\ 0)^*$  SAED pattern of Fig. 3a. They are not well established and can vary slightly from a crystallite to another one leading to the formation of loci, sign of a state intermediate between short and long range orders. More often, extra spots are observed involving a doubling of the  $c$  parameter; the enlargement of Fig. 3b also evidences a small component perpendicular to the  $c$ -axis as the three extra spots are not perfectly aligned (Fig. 3c). The existence of partly established order is also evidenced on the  $(\bar{1}\ 1\ 2)^*$  oriented SAED patterns within a same crystallite: patterns without extra spots (Fig. 4a), patterns with extra spots implying a tripling of the cell along  $[0\ 2\ -1]^*$  (Fig. 4b) or even patterns showing an overlap of zones with and without superstructures (Fig. 4c) can be observed.

To take into account the TEM observations, symmetry was lowered to  $P2_1$  and cell parameters were refined to  $a = 7.3207(5)$  Å;  $b = 7.4553(6)$  Å;  $c = 7.4037(4)$  Å and  $\beta = 118.578(3)$ ° ( $V = 354.849(4)$  Å $^3$ ). Lowering the symmetry to  $P2_1$  involves three iron sites, instead of two, and the inversion centre at Fe2 is lost. The large number of parameters (3 Fe, 1P and 10 O -all in general  $(x, y, z)$  position) compared to the number and intensity of the "extra" Bragg peaks does not allow pushing further the analysis, which was pursued using single crystal SXRD data.

The diffraction data obtained on single crystals (sizes about  $5 \times 6 \times 15$  μm $^3$ ) exhibit good intensity, but poor diffraction quality, with signs of splitting/twinning in some images, in perfect agreement with the numerous defects observed by TEM. As mentioned above, the  $P2_1/n$  has to be ruled out, as  $n$ -glide plane reflection conditions ( $h0l$ :  $h + l = 2n$ ) are violated, as observed also on the  $h0l$  reconstruction of the reciprocal space, where additional super lattice reflections are clearly present, indicating a doubling along the  $c$ -axis (Fig. 5). Synchrotron experiments performed also on larger crystals (sizes about  $30 \times 15 \times 15$  μm $^3$ ) confirm the presence of these satellites but these data did not permit to solve the structure in the large cell, owing to poor crystal quality and low statistics of the  $hkl$  superlattice reflections. Consequently, the structure was solved in the  $P2_1$  supercell, using the higher quality data of a chosen small crystal recorded at 175 K, leading to an agreement factor of 5.75% (Table 1). A polar twin was used giving rise to a Flack parameter of 0.55(5).

From single crystal data, the structure is refined as a supercell with a

doubling of the  $c$  parameter within the  $P2_1$  space group (Fig. 1c). An additional Fe site, perfectly identifiable on the observed Fourier map (Fig. 6), has to be introduced in the framework previously described. This latter Fe7 atom is partly occupied (22 %) and over six other Fe sites are not fully occupied (Tables 2 and 3). Such a non-stoichiometric Fe7 site explains its anomalously large atomic displacement parameter (ADP) (Table 2), and its highly distorted oxygen octahedral environment (Table 4). Hydrogen atoms are bonded to O9 and O15, which are both connected to three iron octahedra. Due to the existence of the non-stoichiometric Fe7, the two last hydrogens could not be placed on O12 and O8. Based on the structure refinement, the stoichiometry of the studied barboselite crystal is found to be  $\text{Fe}_{2.8(1)}(\text{PO}_4)_2(\text{OH})_2$ ; as the residual electron density is rather high, the standard deviation of the iron content is however probably underestimated. Because of the extra non-stoichiometric iron site that statistically connects the trimers in the  $ab$ -plane, the structure can be described as derived from the  $P2_1/n$  one with modulations of the Fe, P and O atomic positions, which can reach a magnitude of 0.027 Å. This additional Fe7 site statistically connects the trimers, as in the  $P4_32_12$  lipscombe polymorph of barboselite (Fig. 1d).

In the ideal theoretical barboselite structure, as already mentioned, there are two iron sites only, which are attributed to ferrous and ferric species regarding the average Fe–O distance of each octahedron. Those  $\langle \text{Fe}–\text{O} \rangle$  reported in Table 4 for the studied crystal do not allow such a clear determination of the iron valence on the seven sites. The structural complexity revealed here by combining TEM and X-ray single crystal diffraction studies was not previously reported [5]. In any case, the refined structural parameters have to be taken cautiously. They correspond to the structure of one single crystal, because of the difficulty to find a crystal giving X-ray diffraction of reasonable quality and, owing to the disorder evidenced by electron diffraction, probably do not truly reflect the average structure.

### 3.2. Magnetic properties

The magnetic susceptibility curves (Fig. 7a) show a magnetic transition at 164 K, below which there is a strong difference between the  $zc$  and  $fc$  modes, in agreement with previous results [15]. The hysteretic behaviour of  $M(H)$  curves (Fig. 7b) indicates ferromagnetic correlations up to 150 K (i.e.  $< T_N$ ) with a very small remnant magnetization, less than  $0.1 \mu\text{B}/\text{f.u.}$  (that is for 4 Fe).

The temperature dependence of the neutron diffractograms, recorded from 1.7 K to RT, shows no structural transition, within the instrumental resolution, but magnetic peaks appear below  $\cong 160$  K (Fig. 8a). The corresponding evolutions of the unit cell parameters and volume (extracted from LeBail fitting using the  $P2_1/n$  cell because of the reduced Q range) vs. temperature are small ( $< 0.35\%$ ). The cell volume  $V$  decreases with decreasing temperature, and only a weak deviation from the Debye law is observed around  $T_N$ . In the same way,  $a$  and  $c$  decrease with temperature, in contrast with the negative thermal expansion (NTE)

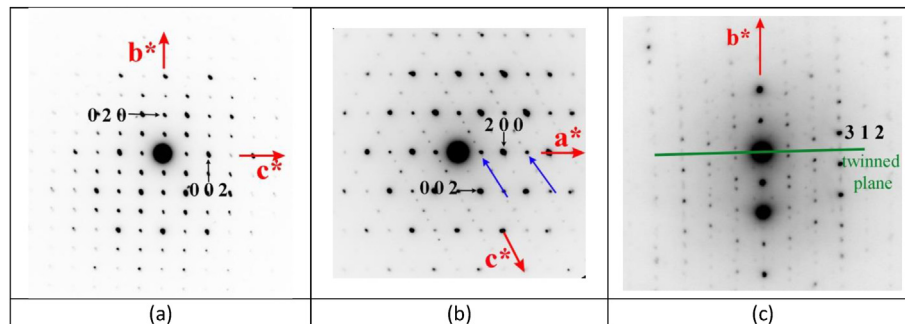
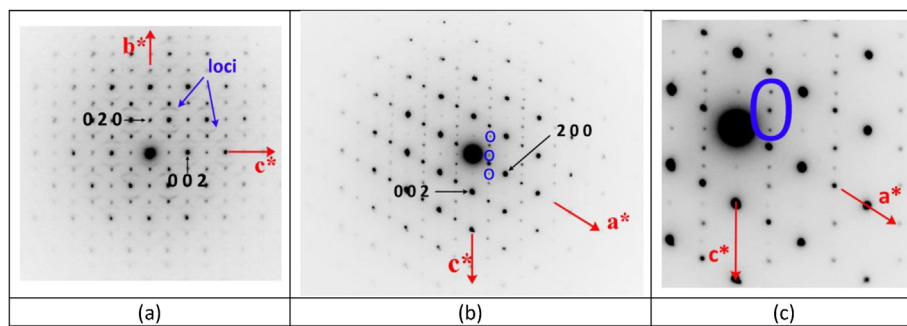
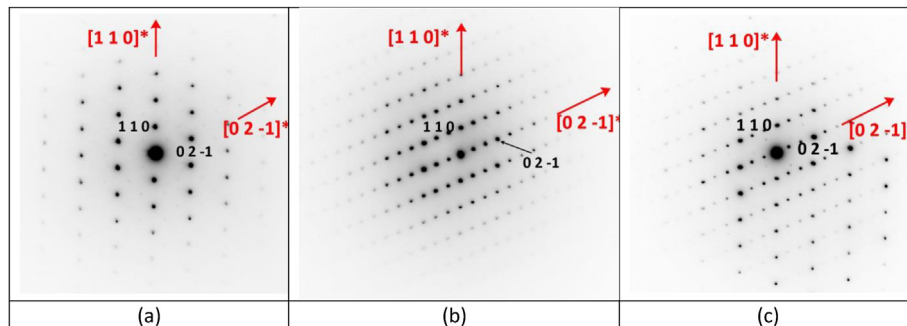


Fig. 2. SAED patterns recorded at RT on  $\text{Fe}_3(\text{PO}_4)_2(\text{OH})_2$  oriented  $(100)^*$  (a),  $(010)^*$  (b) and  $(\bar{2}03)^*$  (c). The blue arrows on the  $(010)^*$  pattern point out the spots incompatible with a  $n$ -glide plane. The green line on Fig. 1c indicates a twinned plane. (For interpretation of the references to colour in this figure legend, the reader is referred to the Web version of this article.)



**Fig. 3.** SAED patterns recorded at RT on  $\text{Fe}_3(\text{PO}_4)_2(\text{OH})_2$  oriented  $(100)^*$  (a), the blue arrows point out the loci due to partial ordering phenomena and  $(010)^*$  (b), the blue ellipses surround extra reflections. **Fig. 2(c)** is an enlargement of **Fig. 2(b)**. (For interpretation of the references to colour in this figure legend, the reader is referred to the Web version of this article.)



**Fig. 4.**  $(\bar{1} 1 2)$  SAED patterns recorded at RT on  $\text{Fe}_3(\text{PO}_4)_2(\text{OH})_2$ , without ordering phenomena (a), implying a tripling along  $[0 2 \bar{1}]^*$  (b) and with an overlap of ordered and non-ordered domains (c).

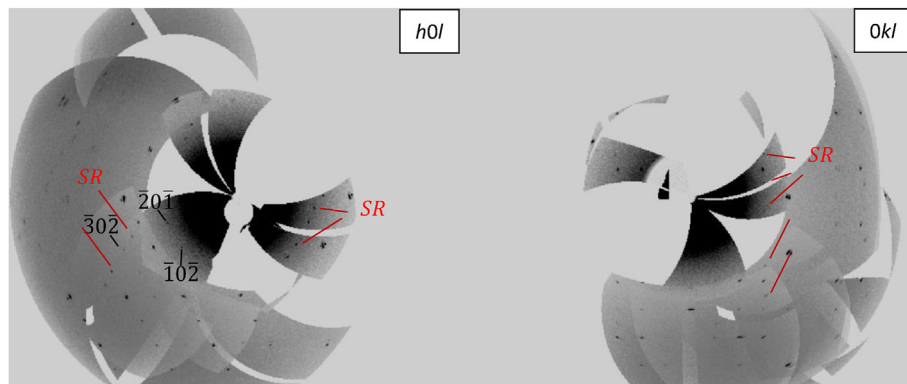


**Fig. 5.**  $h0l$  and  $0kl$  reconstructions of reciprocal space. Reflections (with  $h + 1 = 2n+1$ ) excluding the possibility of  $P2_1/n$  space group and  $1 \times 1 \times 2$  superlattice reflections (SR) are highlighted.

observed along the  $b$ -axis, the  $\beta$  angle remaining nearly constant (Fig. 8b).

For the sake of simplicity, in the first stages of the analysis, the small  $P2_1/n$  cell was used for the magnetic structure determination, to decrease the number of independent atoms in the magnetic cell. Below  $T_N = 160$  K, the magnetic peaks can be indexed with the propagation vector  $\mathbf{k} = 0\ 0\ 0$ . The resolution-limited width of the magnetic Bragg peaks attests of a well-established long range magnetic order. The corresponding magnetic structure at 1.5 K has been determined by Rietveld refinement using symmetry adapted modes derived from a representation analysis performed with the BasIreps program [16].

There are four one-dimensional irreducible representations of the little group  $G_{\mathbf{k}}$  for  $\mathbf{k} = 0\ 0\ 0$ . The magnetic representation  $\Gamma_m$  calculated for the Wyckoff positions of the two independent Fe atom in the  $P2_1/n$  space group is  $\Gamma_m = 3\Gamma_1 \oplus 3\Gamma_3$  for the 2a site and  $\Gamma_m = 3\Gamma_1 \oplus 3\Gamma_2 \oplus 3\Gamma_3 \oplus$

$3\Gamma_4$  for the 4e site, so that there are three basis functions for each representation. Table 5 lists the corresponding basis vectors. The best models were obtained using the single  $\Gamma_1$  irreducible representation for both sites, and mixing components along  $a$  and  $c$ . Although they belong to different Wyckoff sites, the moments of both Fe sites were constrained to be parallel, to limit the number of free parameters in the refinement, owing to the limited number of available magnetic peaks and to the additional difficulty of the  $\mathbf{k} = 0\ 0\ 0$  structure. The refinement was actually not improved significantly by releasing this constraint, in agreement with the random  $\text{Fe}^{2+}/\text{Fe}^{3+}$  distribution. Similarly, adding a magnetic component along  $b$  did not lead to quantifiably better results. The best refinement is illustrated in Fig. 9a, with the corresponding magnetic structure in Fig. 9b. The components of the magnetic moment are  $m_x = 1.5(1) \mu_B$  and  $m_z = 4.8(1) \mu_B$ , that is, nearly perpendicular to the  $ab$  plane (the deviation is  $\approx 10^\circ$ , Fig. 9b). The ordered component

**Table 1**  
Crystal data with  $P2_1$  space group.

	$P2_1$ (#4)
Sum formula	$Fe_{11.5}O_{40}P_8H_4$
$a(\text{\AA})$	7.2878(13)
$b(\text{\AA})$	7.4749(9)
$c(\text{\AA})$	14.793(2)
$B(\text{^\circ})$	118.52(2)
$V(\text{\AA}^3)$	708.1(2)
$Z$	2
$M / \text{mm}^{-3}$	52.718
$\rho_{\text{calc}} / \text{gcm}^{-3}$	3.5967
$F(000)$	742.6
2 $\theta$ range / $^\circ$	6.073–66.672
Index ranges	$-8 \leq h \leq 8, -4 \leq k \leq 8, -17 \leq l \leq 16$
no. of measured reflns	2511 [ $R_{\text{int}} = 0.016$ ]
no. of unique	1361
Average $I/\sigma$	35.46
Data/Restraints/Parameters	2511/0/175
Final R factors [ $I > 2\sigma(I)$ ]/%	5.75
Largest residual peak/hole / $\text{e\AA}^{-3}$	1.889/-0.97
Flack parameter	0.55(5)

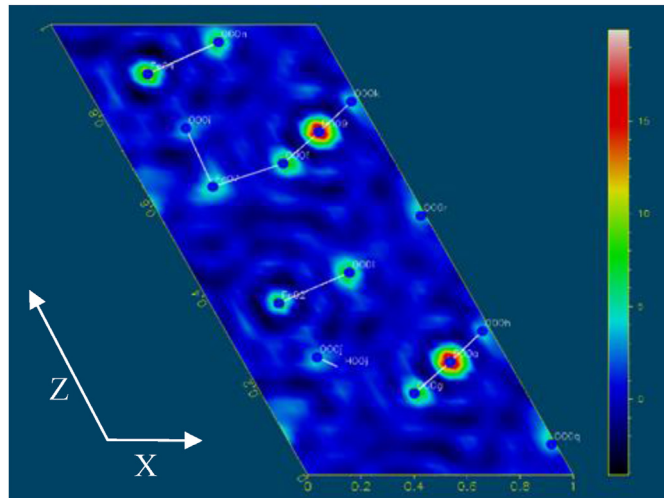


**Fig. 6.** (a) Observed Fourier map at  $y = 0.16$  with the  $P2_1$  crystal structure showing the existence of the  $Fe07$  site. Color scale is in  $\text{e\AA}^{-3}$ . (For interpretation of the references to colour in this figure legend, the reader is referred to the Web version of this article.).

maximum is close to  $4.3 \mu_B$ , i.e. in agreement with the theoretical value of  $4.66 \mu_B$  expected to a nominal  $2\text{Fe}^{+3}:1\text{Fe}^{+2}$  composition taking the spin only value ( $5 \mu_B$  and  $4 \mu_B$  for  $\text{Fe}^{+3}$  and  $\text{Fe}^{+2}$ , respectively). Since the magnetic structure is solved in the small  $P2_1/n$  cell, the value of magnetic moment cannot be discussed further, in particular in link with the small remnant magnetization observed on the  $M(H)$  curves. Within iron trimers, moments are ferromagnetically coupled and surrounding trimers along  $c$  are aligned antiferromagnetically. This average model in the small  $P2_1/n$  cell gives a very satisfactory refinement of the neutron diffraction data; lowering the symmetry to the  $P2_1$  cell doubled along  $c$  with seven independent Fe atoms and unconstrained  $m_x$ ,  $m_y$ , and  $m_z$  components leads to the magnetic space group  $P2_1$  (BNS #4.7). Refinements of the individual  $m_x$  and  $m_z$  components (assuming  $m_y = 0$ ) on each Fe sites were therefore not attempted, owing to the lack of information intrinsic to the powder data. In the larger barboselite cell, the general picture of ferromagnetic planes of Fe trimers coupled AF along  $c$  remains the key feature of the magnetic ordering, with Fe moments arguably varying slightly depending on the site considered. Importantly, the magnetic point group of  $P2_1$  allows non-zero polarisation and linear magneto-electric tensors, making of the barboselite structure a promising candidate for the design of new multiferroics.

**Table 2**

Crystallographic parameters [atomic coordinates (all atoms are in the general ( $x$ ,  $y$ ,  $z$ )  $2a$  Wyckoff site), site occupancy factors (Occ), and equivalent isotropic ( $U_{\text{eq}}$ ) atomic displacement parameters ( $\text{\AA}^2$ )] of  $Fe_3(PO_4)_2(OH)_2$  at 175 K. Hydrogen atom generation was performed with OH distance =  $0.98 \text{\AA}$  and ADP arbitrarily fixed at  $0.5 \text{\AA}^2$ .

	$x$	$y$	$z$	Occ	$U_{\text{eq}}$
Fe1	0.4727(5)	0.4615(8)	0.1199(3)	0.93(2)	0.0096(10)
Fe2	0.7511(7)	0.7318(9)	0.6264(4)	0.85(2)	0.0068(8)
Fe3	0.5237(5)	0.9627	0.3785(3)	1	0.0144(10)
Fe4	-0.2478(7)	0.7302(8)	0.1272(3)	1	0.0150(8)
Fe5	0.9780(6)	0.4963(7)	0.3730(3)	0.85(2)	0.0085(10)
Fe6	0.0231(6)	0.9962(7)	0.1276(3)	0.91(2)	0.0094(9)
Fe7	1.250(5)	0.180(5)	0.628(3)	0.22(3)	0.078(9)
P1	0.2467(10)	0.8425(17)	-0.0020(4)	1	0.0155(15)
P2	0.7550(10)	0.3428(17)	0.5026(4)	1	0.0147(15)
P3	0.2520(12)	0.6127(14)	0.2533(4)	1	0.0120(13)
P4	0.7474(12)	0.1134(14)	0.2462(5)	1	0.0137(14)
O1	0.202(2)	0.957(3)	0.0676(12)	1	0.016(4)
O2	0.692(2)	0.456(2)	0.5730(11)	1	0.011(3)
O3	0.800(3)	0.458(3)	0.4346(13)	1	0.022(4)
O4	0.310(2)	0.956(2)	-0.0711(11)	1	0.010(3)
O5	0.448(2)	0.718(2)	0.3218(11)	1	0.009(3)
O6	0.552(2)	0.218(2)	0.1775(12)	1	0.012(3)
O7	0.926(3)	0.232(3)	0.3130(13)	1	0.020(4)
O8	0.726(3)	0.591(3)	0.2453(12)	1	0.010(4)
O9	0.724(3)	0.591(3)	0.7439(12)	1	0.012(4)
H1	0.6578	0.6764	0.7698	1	0.5
O10	0.073(2)	0.731(2)	0.1874(12)	1	0.014(4)
O11	0.567(2)	0.209(3)	0.4402(11)	1	0.011(3)
O12	0.762(3)	0.859(4)	0.5003(13)	1	0.028(5)
O13	0.430(2)	0.708(3)	0.0578(11)	1	0.013(3)
O14	0.183(3)	0.487(3)	0.3151(14)	1	0.027(4)
O15	0.227(3)	0.359(4)	-0.0077(13)	1	0.024(5)
H2	0.1618	0.2724	0.0178	1	0.5
O16	0.058(3)	0.722(3)	-0.0667(13)	1	0.021(4)
O17	0.942(3)	0.220(3)	0.5639(13)	1	0.020(4)
O18	0.303(2)	0.483(3)	0.1881(13)	1	0.020(4)
O19	0.815(3)	-0.012(3)	0.1858(13)	1	0.021(4)
O20	0.700(2)	-0.014(3)	0.3125(12)	1	0.015(4)

#### 4. Discussion and conclusion

The monoclinic structure proposed initially for the barboselite  $Fe_3(PO_4)_2(OH)_2$  [15] is characterised by the existence of  $Fe^{3+}$ - $Fe^{2+}$ - $Fe^{3+}$  “trimers”, also-called h-clusters, specific to iron phosphates materials [19], with short Fe-Fe equal distances within the trimers; those trimers are themselves connected by  $PO_4$  tetrahedra, leading to a dense structural arrangement. In this structural framework, disorder is observed by TEM, with the existence and coexistence of several types of super structures and defects as twins. This is confirmed by a single crystal analysis showing a double cell with an extra Fe site, leading to a distribution of iron on seven crystallographic sites and thus to a distribution of Fe-O distances and probably to a distribution of iron valence states incompatible with  $Fe^{3+}$ - $Fe^{2+}$  long range charge ordering.

This arrangement in clusters of face-sharing  $Fe_6$  octahedra is common to barboselite and lipscomite, which have the same composition. Barboselite may be considered as an ordered equivalent of the  $P4_12_12$  lipscomite, having “isolated” 3Fe-clusters instead of chains. Indeed, the lipscomite structure is composed of face sharing  $Fe_6$  octahedra according to the scheme  $Fe1$ - $Fe3$ - $Fe2$ - $Fe3$ - $Fe1$ , with an occupancy factor of 0.47 for  $Fe1$  and  $Fe2$ . As in barboselite, the chains are interconnected by  $PO_4$  tetrahedra [19,20] (Fig. 1d). The fact that there is a close structural relationship between the barboselite and lipscomite crystal structures is also further confirmed by the barboselite to lipscomite transition observed when annealing in air.

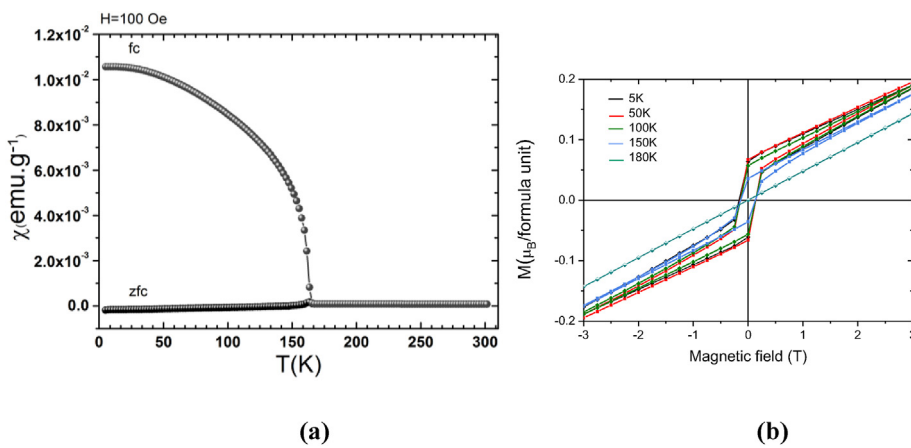
The studied single crystal appears thus as an intermediate case between the perfect iron order and disorder of barboselite and lipscomite, respectively. It is clear that several types of super cells exist, as demonstrated by TEM observations, which probably correspond to the stabilization of other iron distribution. The arrangement of iron face-sharing

**Table 3**Atomic displacement parameters of  $\text{Fe}_2\text{Fe}(\text{PO}_4)_2(\text{OH})_2$  corresponding to **Table 2** ( $U_{ij}$   $\text{\AA}^2$ ).

	$U_{11}$	$U_{22}$	$U_{33}$	$U_{23}$	$U_{13}$	$U_{12}$
Fe1	0.0081(16)	0.010(2)	0.0044(15)	-0.0031(15)	-0.002(2)	-0.002(2)
Fe2	0.0084(15)	0.0024(18)	0.0102(14)	0.0033(14)	0.0049(12)	0.0019(13)
Fe3	0.0133(17)	0.018(3)	0.0045(14)	-0.0051(15)	-0.002(2)	-0.004(2)
Fe4	0.0155(15)	0.0146(19)	0.0043(12)	-0.0021(13)	-0.004(1)	-0.002(1)
Fe5	0.0123(18)	0.002(2)	0.0143(18)	-0.0012(17)	0.0092(16)	-0.003(2)
Fe6	0.0098(16)	0.009(2)	0.0056(15)	-0.0016(16)	0.0006(14)	-0.001(2)
P1	0.014(3)	0.021(4)	0.010(3)	0.000(2)	0.005(2)	0.000(3)
P2	0.012(3)	0.024(4)	0.007(3)	-0.003(2)	0.004(2)	-0.003(3)
P3	0.015(3)	0.006(2)	0.008(2)	-0.001(2)	-0.002(2)	-0.003(3)
P4	0.015(3)	0.007(3)	0.014(3)	0.001(3)	0.003(2)	0.003(3)

**Table 4**Interatomic distances ( $\text{\AA}$ ) corresponding to **Table 2** (Fe and P are in octahedral (Oh) and tetrahedral (Td) environments, respectively), the average Fe–O distance in each octahedron is given in the last column.

Fe1	O18 1.942(17)	O6 1.972(18)	O15 2.03(2)	O4 2.031(15)	O13 2.016(19)	O8 2.125(18)	<2.019>
Fe2	O11 2.046(15)	O14 2.05(2)	O7 2.080(17)	O9 2.118(19)	O12 2.13(2)	O2 2.174(18)	<2.100>
Fe3	O20 1.956(16)	O12 1.97(2)	O5 1.977(17)	O2 2.018(15)	O11 2.010(18)	O9 2.083(18)	<2.002>
Fe4	O10 2.067(15)	O13 2.070(15)	O15 2.08(2)	O19 2.07(2)	O8 2.120(18)	O4 2.179(18)	<2.098>
Fe5	O17 1.87(2)	O3 1.929(18)	O8 2.032(19)	O14 2.050(19)	O7 2.125(19)	O12 2.125(19)	<2.031>
Fe6	O16 1.87(2)	O1 1.921(16)	O9 2.042(19)	O19 2.071(17)	O10 2.127(18)	O15 2.10(2)	<2.022>
Fe7	O3 1.84(4)	O8 1.92(4)	O5 1.98(3)	O17 2.00(4)	O12 2.29(4)	O20 2.44(6)	<2.078>
P1	O1 1.488(19)	O13 1.54(2)	O16 1.556(17)	O4 1.566(18)			
P2	O3 1.48(2)	O17 1.53(2)	O11 1.570(17)	O2 1.590(18)			
P3	O5 1.518(17)	O10 1.492(18)	O14 1.55(2)	O18 1.53(2)			
P4	O6 1.516(18)	O7 1.493(19)	O20 1.52(2)	O19 1.53(2)			

**Fig. 7.** (a) Evolution with temperature of the magnetic susceptibility  $\chi(T)$  of  $\text{Fe}_3(\text{PO}_4)_2(\text{OH})_2$ , recorded in 100 Oe in zfc and fc modes. (b) Magnetization curves at 5 K, 50 K, 100 K, 150 K and 180 K.

octahedra trimers, combined with a distribution of iron site occupancies, allows various lattices to be built. The complexity of the crystal chemistry of the iron phosphates was already underlined by P.B. Moore in 1970 [19]. It also explains why different chemical formula and symmetries

have been reported in the literature for both natural and synthetic lipso-combite samples for instance. More generally, the quaternary system  $\text{FeO}-\text{Fe}_2\text{O}_3-\text{P}_2\text{O}_5-\text{H}_2\text{O}$  is very rich and complex, due to the huge number of phases it contains and to the relationships between them [21,22].

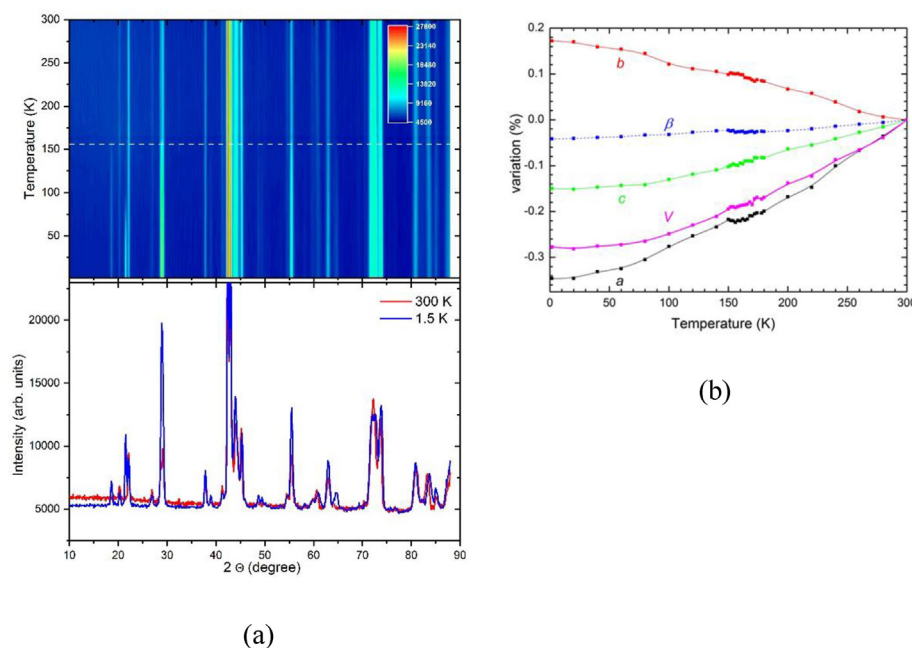


**Fig. 8.** (a) Neutron powder diffraction patterns of barbosalite vs. temperature, from 1.5 to 300 K ( $\lambda = 2.427 \text{ \AA}$ , G4.1 diffractometer at LLB) (top). Superposition of the corresponding 1.5 and 300 K patterns (bottom). (b) Relative evolution of unit cell parameters for barbosalite from neutron diffraction data ( $P2_1/n$  space group) between 1.5 K and 300 K.

**Table 5**

Basis functions for axial vectors associated with irreducible representations  $\Gamma_1$  for Wyckoff site 2a and 4e in  $P2_1/n$  space group.

$\Gamma_1$	$(x, y, -x+\frac{1}{2}, z)$	$(x, y, (x+\frac{1}{2}, y-\frac{1}{2}, -z+\frac{1}{2})$	$(-x+1, -y+1, -y+3/2, -z+\frac{1}{2})$	$(x+\frac{1}{2}, -y+1, -y+3/2, -z+\frac{1}{2})$
$\text{Fe}_{11}$	$(-z+\frac{1}{2})$	$\text{Fe}_{21}$	$\text{Fe}_{22}$	$\text{Fe}_{23}$
$\text{Fe}_{12}$				$\text{Fe}_{24}$
$\psi_1$	$(1 \ 0 \ 0)$	$(1 \ 0 \ 0)$	$(-1 \ 0 \ 0)$	$(1 \ 0 \ 0)$
	$(0 \ 0 \ 0)$		$(0 \ 0 \ 0)$	$(-1 \ 0 \ 0)$
$\psi_2$	$(0 \ 1 \ 0)$	$(0 \ 1 \ 0)$	$(0 \ 1 \ 0)$	$(0 \ 1 \ 0)$
	$(0 \ 0 \ 0)$		$(0 \ 0 \ 0)$	$(0 \ 1 \ 0)$
$\psi_3$	$(0 \ 0 \ -1)$	$(0 \ 0 \ -1)$	$(0 \ 0 \ -1)$	$(0 \ 0 \ -1)$
	$(0 \ 1 \ 0)$		$(0 \ 1 \ 0)$	$(0 \ 0 \ -1)$

Even if the description based on Fe-trimers for barbosalite and derived structures is pertinent, depending on the compounds the average sizes of  $\text{FeO}_6$  octahedra and their distortions strongly vary, requiring spectroscopy for identification of the ferrous and ferric species. The OH group probably plays also a role on the ferric and ferrous cations ordering, referring to the phases obtained after catalytic reaction that

belong to the  $\text{Fe}_{4+2x}(\text{PO}_4)_3(\text{OH})_{3-3x}\text{O}_{3x}$  solid solution (with  $0 \leq x \leq 1$ ) [6].

Concerning the magnetic ordering, the fact that long-range antiferromagnetism is evidenced in this study demonstrates that the structural complexity with 7 Fe sites not all fully occupied, detrimental to the charge ordering, has actually little impact on magnetic exchanges.

This strongly supports that Fe–O–Fe superexchange is strong in that compound.

Interestingly, in  $\text{Fe}_3\text{BO}_5$ , multiferroicity was preserved by Mn substitution, although  $\text{Fe}^{2+}$ – $\text{Fe}^{3+}$  charge ordering was also suppressed [14]. The origin of the spontaneous polarisation which appears below  $T_N$  in the ludwigite compounds is still an open question, as it could be linked with a polar disorder of charges in the structure. In all cases, it would be interesting to measure the electrical polarisation of barbosalite as a function of temperature or/and magnetic field in order to check the magnetoelectric coupling predicted by the symmetry analysis of the magnetic structure.

#### Declaration of competing interest

The authors declare that they have no known competing financial

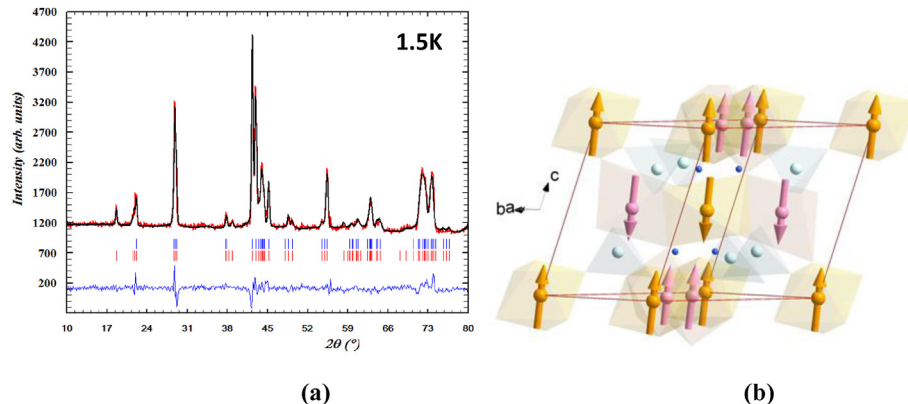


**Fig. 9.** (a) Rietveld refinement results (experimental data: open circles, calculated profile: continuous line, allowed Bragg reflections: vertical marks. The first and second rows of marks correspond to the crystal and magnetic Bragg peak positions, respectively. The difference between the experimental and calculated profiles is displayed at the bottom of the graph.) of the 1.5 K neutron diffraction data (G4.1) of  $\text{Fe}_3(\text{PO}_4)_2(\text{OH})_2$ . (b) Corresponding magnetic structure of  $\text{Fe}_3(\text{PO}_4)_2(\text{OH})_2$  at 1.5 K.

interests or personal relationships that could have appeared to influence the work reported in this paper.

### CRediT authorship contribution statement

**M. Poienar:** Conceptualization, Funding acquisition, Project administration, Writing - original draft, Validation, Formal analysis, Investigation. **F. Damay:** Writing - review & editing, Validation, Formal analysis, Investigation. **J. Rouquette:** Writing - review & editing, Validation, Formal analysis, Investigation. **V. Ranieri:** Validation, Formal analysis, Investigation. **S. Malo:** Validation, Formal analysis, Investigation. **A. Maignan:** Supervision, Writing - review & editing, Validation, Formal analysis, Investigation. **E. Elkäim:** Validation, Formal analysis, Investigation. **J. Haines:** Validation, Formal analysis, Investigation. **C. Martin:** Supervision, Writing - original draft, Writing - review & editing, Validation, Formal analysis, Investigation.

### Acknowledgement

Financial support for this work was provided by the joint French-Romanian project ANR-UEFISCDI, contracts no. 8 RO-FR/01.01.2013, code PN-II-ID-JRP-2011-2-0056/ ANR-12-IS08-0003, COFeIn. This work is dedicated to our colleague Dr R. Baies<sup>†</sup>, from Timișoara, who was involved in the early stage of this work.

### References

- [1] J. Chen, Recent progress in advanced materials for lithium ion batteries, *Materials* 6 (2013) 156–183.
- [2] C. Masquelier, A.K. Padhi, K.S. Nanjundaswamy, J.B. Goodenough, New cathode materials for rechargeable lithium batteries: the 3-D framework structures  $\text{Li}_3\text{Fe}_2(\text{XO}_4)_3$  (X=P, as), *J. Solid State Chem.* 135 (1998) 228–234.
- [3] K.S. Nanjundaswamy, A.K. Padhi, J.B. Goodenough, S. Okada, H. Ohtsuka, H. Arai, J. Yamaki, Synthesis, redox potential evaluation and electrochemical characteristics of NASICON-related-3D framework compounds, *Solid State Ionics* 92 (1996) 1–10.
- [4] A.K. Padhi, K.S. Nanjundaswamy, J.B. Goodenough, Phospho-olivines as positive-electrode materials for rechargeable lithium batteries, *J. Electrochem. Soc.* 144 (1997) 1188–1194.
- [5] P. Sandineni, K. Ghosh, A. Choudhury, Electrochemistry of illusive barboselite,  $\text{Fe}^{2+}\text{Fe}^{3+}_2(\text{PO}_4)_2(\text{OH})_2$ : an iron phosphate related to lipscomite structure, *J. Electrochem. Soc.* 166 (2019) A3585.
- [6] D. Rouzies, J.M.M. Millet, D. Siew Hew Sam, J.C. Vedrine, Isobutyric acid oxidative dehydrogenation over iron hydroxyphosphates. I. Catalytic properties and role of water, *Appl. Catal. Gen.* 124 (1995) 189–203.
- [7] J.M.M. Millet, D. Rouzies, J.C. Vedrine, Isobutyric acid oxidative dehydrogenation over iron hydroxyphosphates. II. Tentative description of the catalytic sites based on Mossbauer spectroscopic study, *Appl. Catal. Gen.* 124 (1995) 205–219.
- [8] G. Rousse, J. Rodriguez-Carvajal, S. Patoux, C. Masquelier, Magnetic structures of the triphylite  $\text{LiFePO}_4$  and of its delithiated form  $\text{FePO}_4$ , *Chem. Mater.* 15 (2003) 4082–4090.
- [9] R. Toft-Petersen, M. Reehuis, T.B.S. Jensen, N.H. Andersen, J. Jiyiing Li, M.D. Le, M. Laver, C. Niedermayer, B. Klemke, K. Lefmann, D. Vaknin, Anomalous magnetic structure and spin dynamics in magnetoelectric  $\text{LiFePO}_4$ , *Phys. Rev. B Condens. Matter* 92 (2015), 024404.
- [10] M. Mercier, J. Gareyt, E.F. Bertaut, Une nouvelle famille de corps magnétocélectriques  $\text{LiMPO}_4$  (M= Mn, Co, Ni), *C. R. Acad. Sci. Ser. B* 264 (1967) 979.
- [11] I. Kornev, M. Bichurin, J.-P. Rivera, S. Gentil, H. Schmid, A.G.M. Jansen, P. Wyder, Magnetoelectric properties of  $\text{LiCoPO}_4$  and  $\text{LiNiPO}_4$ , *Phys. Rev. B Condens. Matter* 62 (2000) 12247.
- [12] M. Lindberg, C.L. Christ, Crystal structures of the isostructural minerals lazulite, scorzalite and barboselite, *Acta Crystallogr.* 12 (1959) 695–697.
- [13] D. Rouzies, J.M.M. Millet, Mossbauer spectroscopic study of synthetic lipscomite and barboselite at room temperature, *Hyperfine Interact.* 77 (1993) 11–18.
- [14] A. Maignan, F. Lainé, A. Guesdon, S. Malo, F. Damay, C. Martin, Charge ordering and multiferroicity in  $\text{Fe}_3\text{BO}_5$  and  $\text{Fe}_2\text{MnBO}_5$  oxyborates, *J. Solid State Chem.* 246 (2017) 209–213.
- [15] G.J. Redhammer, G. Tippelt, G. Roth, W. Lottermoser, G. Amthauer, Structure and Mossbauer spectroscopy of barboselite  $\text{Fe}^{2+}\text{Fe}^{3+}_2(\text{PO}_4)_2(\text{OH})_2$  between 80 K and 300 K, *Phys. Chem. Miner.* 27 (2000) 419–429.
- [16] J. Rodriguez-Carvajal, Recent advances in magnetic structure determination by neutron powder diffraction, *Phys. B Condens. Matter.* 192 (1993) 55–69.
- [17] G.M. Sheldrick, A short history of SHELX, *Acta Crystallogr. A Found. Crystallogr.* 64 (2008) 112–122.
- [18] C.C. Torardi, M. Reiff, I. Takacs, Crystal structure, and magnetism of  $\text{Fe}_4(\text{OH})_3(\text{PO}_4)_3$  and  $\text{V}_4\text{O}(\text{OH})_2(\text{PO}_4)_2$ : chains of  $\text{M}_2\text{O}_9$  dimers connected by hydroxyl groups, *J. Solid State Chem.* 82 (1989) 203–215.
- [19] P.B. Moore, Crystal chemistry of the basic iron phosphate, *Am. Mineral.* 55 (1970) 135–169.
- [20] I. Vencato, E. Mattievich, Y.P. Mascarenhas, Crystal structure of synthetic lipscomite: a redetermination, *Am. Mineral.* 74 (1989) 456–460.
- [21] P. Schmid-Beurmann, Stability properties and phase relations of  $\text{Fe}^{3+}\text{Fe}^{2+}_2(\text{PO}_4)_3(\text{OH})_{3-3x}\text{O}_{3x}$  in the quaternary system  $\text{FeO-Fe}_2\text{O}_3\text{P}_2\text{O}_5\text{H}_2\text{O}$ , *J. Mater. Chem.* 11 (2001) 660–667.
- [22] P. Schmid-Beurmann, Synthesis and phase characterization of a solid solution series between  $\beta\text{-Fe}_2(\text{PO}_4)_O$  and  $\text{Fe}_4(\text{PO}_4)_3(\text{OH})_3$ , *J. Solid State Chem.* 153 (2000) 237–247.